archives
of thermodynamics
Vol. **44**(2023), No. 3, 217–240
DOI: 10.24425/ather.2023.147545

Experimental and numerical analysis of vortex generators designed for utility vehicles

RAMESH KUMAR CHIDAMBARAM[a]
RAJESH KANNA[b*]
POOMANANDAN GOPAL[c]
SENTHIL KUMAR ARUMUGAM[d]

[a] Vellore Institute of Technology, Automotive Research Centre, Vellore – 632014, India

[b] Vellore Institute of Technology, CO_2 Research and Green Technologies Center, Vellore – 632014, India

[c] Anna University, Department of Automobile Engineering, BIT Campus, Tiruchirappalli, 620024, India

[d] VIT Bhopal University, Bhopal, 466114, India

Abstract The main goal of today's car designers is to minimize fuel consumption in all possible ways at the same time maintaining the vehicle's performance as usual. The goal of this work is to study the effect of adding a vortex generator (VG) on the aerodynamics of the vehicle and fuel economy. Both theoretical and experimental works were carried out and the outcomes of the numerical simulations are contrasted with those of the experimental results. A utility vehicle model with a scale ratio of 1:15 was used as a test model. Experimental research has been done on the fluctuation of the coefficient of pressure, dynamic pressure, and coefficients of lift and drag with and without VG on the roof of a utility vehicle. The delta-shaped VG was put to the test both numerically and experimentally. At a velocity of 2.42 m/s, it is observed that the addition of VG can raise the pressure coefficient by about 17%. When compared to the vehicle model without vortex generators, the velocity profile of the ccomputational fluid dynamics analysis shows that at the back end of the vehicle, the wake has been minimized with VG.

Keywords: Vortex generator; Pressure coefficient; Numerical simulation; Drag force

*Corresponding Author. Email: prkanna@gmail.com

Nomenclature

A	–	projected area, m^2
C_D	–	coefficient of drag
C_L	–	coefficient of lift
C_p	–	pressure coefficient
D	–	drag force, N
H	–	height, m
I/H	–	interval to height ratio
L	–	lift force, N
p	–	static pressure, N/m^2
P_d	–	dynamic pressure, N/m^2
p_∞	–	total pressure, N/m^2
Re	–	Reynolds number
S_i	–	user-defined source term
S_{ij}	–	strain tensor
t	–	time, s
U_∞	–	velocity of air, m/s
u	–	relative speed of air, m/s
u_i	–	components of velocity in x_i-direction, m/s
x	–	coordinate along scale model centreline, mm
x_i	–	Cartesian coordinates, m

Greek symbols

α	–	yaw angle, deg
ρ_∞	–	density of air, kg/m^3
δ_{ij}	–	stress sensor
μ	–	viscosity

Acronyms

CFD	–	computational fluid dynamics
VG	–	vortex generator

1 Introduction

An aerodynamic component known as a vortex generator (VG) is a tiny vane attached to a body to produce a vortex. They are used in a variety of applications, including those in road vehicles, ships, turbines, and aircraft wigs [1]. To keep the airflow constant over the control surfaces at the back of the moving wing or a body, vortex generators are used. They are often made in a rectangular or triangular shape to a size of 10 to 20 mm [2]. For passive control of shock Wave/boundary-layer interactions, vortex generators are researched by both theoretical and experimental methods by

researchers [3,4]. The exact methods by which they operate at high speeds are still a debate [5,6].

The review of the literature shows that vortex generators (VGs) alter the boundary layer's internal structure to increase its resistance to separation. Some researchers contend that the mixing of the free stream with the trailing vortices energizes the boundary layer[7, 8]. However, it would appear that no experimental or computational findings have been made to back up this assertion. The compactness of VGs provides a practical advantage over their conventional counterparts [9,10].

Generally, analyzing the flow over an object with add-on devices like a vortex generator in a wind tunnel is expensive [11,12]. The cost of the wind tunnel, measuring equipment and the number of test runs necessary for add-on device optimization for drag reduction is money and time-consuming. These expenses can be eliminated by using computational fluid dynamics (CFD) simulations. Aerodynamic simulation utilising offers a quicker turnaround time and will only cost a fraction of the price of the wind tunnel or road testing today due to the decrease in computational cost as well. The Reynolds-averaged Navier–Stokes equations (RANS equations) and turbulence modelling equations can thus be solved to analyse the flow over vehicles and produce results that are close to realistic [13,14].

The amount of power needed for a car travelling at constant speed on a flat road to overcome tyre rolling resistance is about 20% of engine output and aerodynamic drag is about 80% of engine output. While the rolling resistance nearly stays constant as speed increases, the power required to overcome aerodynamic resistance (drag) increases dramatically with the vehicle speed as shown by the relationship

$$\text{Power}_{(\text{Required})} = \frac{1}{2} C_D \rho_\infty A U_\infty^3 \,. \tag{1}$$

Though fuel-saving technology has been the main focus of both vehicle manufacturers and researchers, studying the aerodynamic impacts of vehicles is crucial given the considerable increase in passenger cars around the world. So this study's main goal is to look at the influence of adding a VG on aerodynamics and fuel consumption. Before conducting the experimental studies, to check the merit of the VGs to reduce drag, a CFD analysis of the flow above utility vehicles with vortex generators with different interval to height (I/H) ratios was also carried out. Followed by the theoretical study, the fluctuation of the static pressure, dynamic pressure, and coefficients of lift and drag with and without vortex generators (VG) on the roof

of a utility vehicle has been experimentally explored in the current work at varied I/H ratios of VG. This work focuses on researching aerodynamic drag as well as generated lift caused by airflow over the vehicle at various free-stream velocities.

2 Experimental details

2.1 Design of vortex generator

To establish a feasible configuration of a vortex generator the determination of the design aspects (variables) for the construction of a VG is essential. Based on the analysis and suggestions from earlier studies, most of the variables were fixed or the degrees of freedom is limited [15]. The shape selected for this study was a single vane-type delta (triangular). Due to their simplicity and widespread usage vane type VGs are more appropriate for installing to the vehicle body. The most typical application of delta-shaped VGs was on aircraft wings [16]. Based on the presumption that the ideal height of the VG would be almost equal to the boundary layer thickness, the thickness of the boundary layer is measured in relation to height [17]. The velocity profile on the car's roof is depicted in Fig. 1. According to Fig. 1, the boundary layer thickness is found to be around 2 mm at the roof end directly in front of the separation point. The ideal height for the VG is therefore thought to be up to about 2 mm. To create a stiffer construction, the VG thickness was maintained at 0.5 mm. The length was measured in relation to the VG's height. In these experimental VGs, the length-to-height

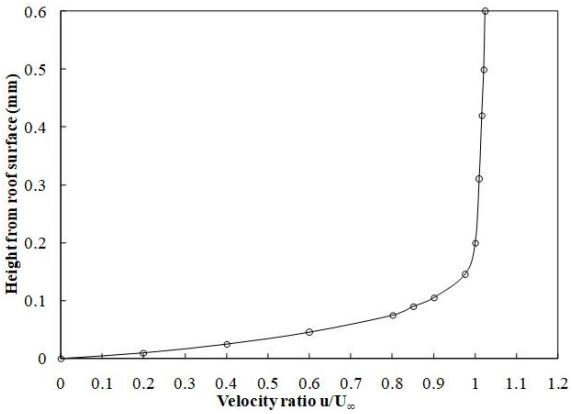

Figure 1: Velocity profile on roof.

ratio is 2, and the yaw angle is 15° to the direction of the airflow. This ratio was used to arrange a single row of VG with 8 members of VG on the roof, as illustrated in Fig. 2.

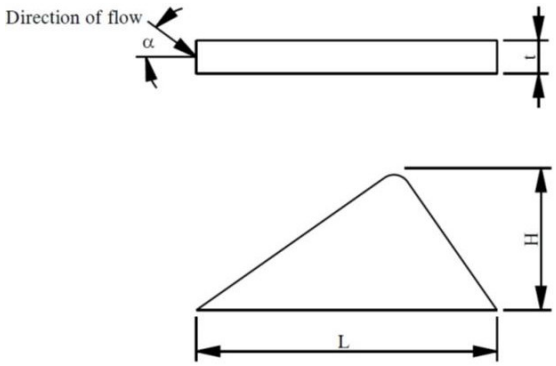

Figure 2: Dimensions of the vortex generator.

The distance (I) between each VG in a row is described in this paragraph. At 5 mm from the end of the roof, one row of VG was mounted. Based on measurements of the boundary layer and the streamline's separation point on the roof, this position was fixed. To reduce weight and potential production costs, there was only one row installed with different I/H ratios of 5, 6, and 7, the delta-shaped VGs. However, it was observed that the direction of wind varied at the side points on the roof. At the centre of a vehicle, the airflow is parallel to the backward direction and gradually deviates towards the centre as the measurement point moves away from the centre. Figure 3 depicts the way of arrangement of vortex generators.

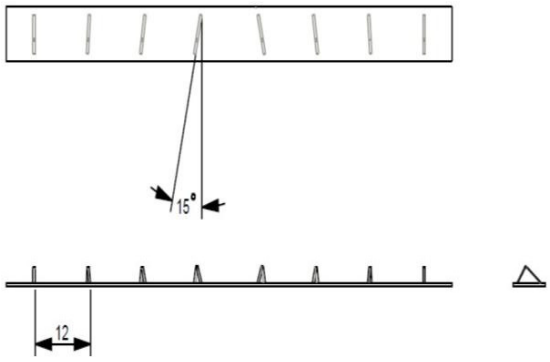

Figure 3: Arrangement of vortex generators in a row.

2.2 Experimental model

A utility vehicle model with a scale ratio of 1:15 was the test model used for this study. Figure 4 depicts the vehicle's scale model. The scaled model measured 0.290 m in length, 0.108 m in width, and 0.1 m in height. A 0.5 mm thick galvanised sheet metal was used to make this model. The same sheet metal was used to create the vortex generators, which were cut into pieces and gas welded onto a base plate. A fastener was used to secure the base plate to the scaled model's roof.

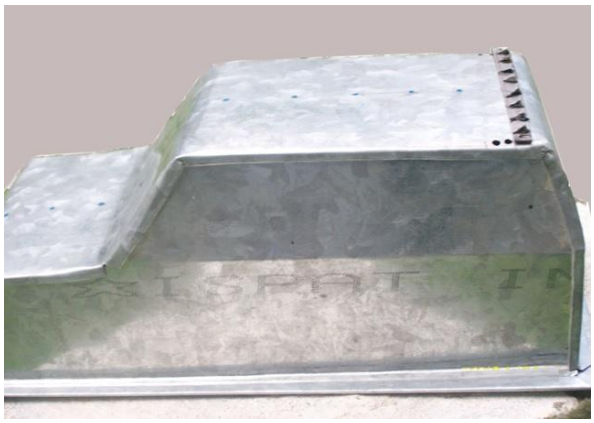

Figure 4: Scale model.

As illustrated in Fig. 5, 0.2 mm diameter holes were made on the vehicle body's centre line starting from the front end to the back end of the vehicle to measure the static pressure above the body. There are 15 pressure tapings

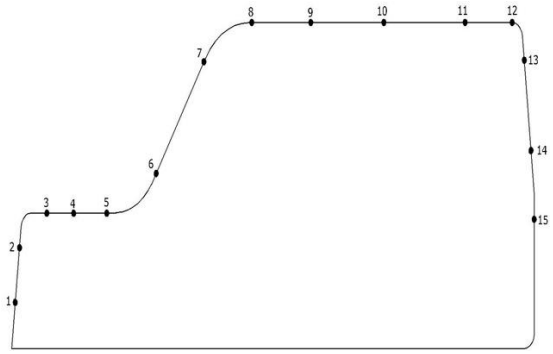

Figure 5: Location of pressure taps.

randomly employed, the roof of the car had five tapings, three of them on the back, and seven on the front. These tapings are bonded with the help of metal paste from the bottom side of the model with the sheet metal surface. Silicone tubes are used to connect the pressure tappings to a 20-way single selection box (like a multiplexer), which is followed by a digital manometer, where the pressure difference is then measured.

The test section of an open circuit wind tunnel (Altech, India) [18] was 0.09 m^2. Figure 6 depicts the wind tunnel's schematic layout. The test section's length was 1 m, while the wind tunnel's overall length was 6 m. For suction, a 2.5 HP electric motor was employed. The yaw angles used in the wind tunnel testing ranged from 15° in both directions. The scale model of the car has a frontal area of 0.0108 m^2. Concerning the model, it is estimated that the blockage ratio is around 9.2% of the test section. In the test part of a wind tunnel, a micromanometer (Furnace Control Ltd.) was used to measure the relative airspeed. The dynamic pressure fluctuations along the centre line of the vehicle body were calculated using this relative air speed measurement. The accuracy of a micromanometer is 0.5%. According to the SAE Wind Tunnel Test protocol, the velocity uniformity is 0.96% or 1% [19].

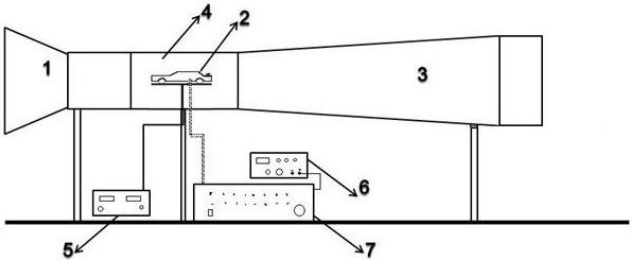

Figure 6: Experimental setup: 1 – air filter, 2 – car model, 3 – axial fan duct, 4 – test section, 5 – force display unit, 6 – micromanometr, 7 – 20-line single way selection box.

The experiment's main goal was to evaluate the drag force, pressure fluctuations, and relative speed on the front, roof, and back along the centre line at different wind speeds. The test model is mounted on a platform which is fastened to a three-axis load cell which enables the measurement of drag and lift force. Figure 7 shows the photographic view of the mount. This load cell converts the variation in position caused by force into an equivalent change in resistance. The output of the load cell is connected to a display unit.

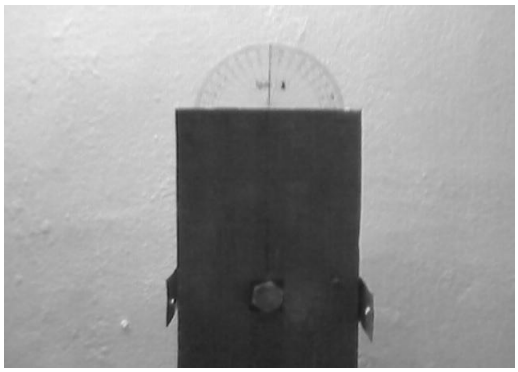

Figure 7: Platform on which model is fixed.

2.3 Experimental analysis

The pressure coefficient (C_P) which is a dimensionless quantity characterises the relative pressures present throughout a flow field. For the study of the low-speed flow of compressible fluids like air, the pressure coefficient is a helpful metric. The relationship between the dimensional parameters and the dimensionless coefficient is as follows:

$$C_p = \frac{p - p_\infty}{\rho_\infty U_\infty^2}\,, \tag{2}$$

where p_∞, U_∞, and ρ_∞ are the total pressure, air velocity and density of air, respectively.

The Bernoulli equation for incompressible flow yields the dynamic pressure (P_d), which is given by

$$P_d = p + \frac{\rho_\infty}{2} u^2. \tag{3}$$

In the equation above, pressure (p) and speed (u) along a streamline are related. The total pressure, according to Bernoulli's equation, is the sum of static and dynamic pressure. In places with high local velocities, the equation predicts low pressure, and *vice versa*. The resultant force that is parallel to and opposes the flow is known as the drag force (D). The drag coefficient (C_D) is calculated empirically, which allows the results to be independent of the actual vehicle dimensions. Drag is related to the drag coefficient as follows:

$$D = \frac{1}{2} C_D \rho_\infty A U_\infty^2\,. \tag{4}$$

The part of the resulting force that is perpendicular to and in opposition to the flow is known as the lift force (L). The relationship between lift force and the force of the relative fluid,

$$L = \frac{1}{2} C_L \rho_\infty A U_\infty^2 \,, \tag{5}$$

is represented by the value of C_L.

2.4 Computational fluid dynamics analysis

Without much expense and time, CFD techniques can be effectively used to visualize the flow pattern of the geometry or fluid flow over a surface when the flow is laminar. When the flow becomes turbulent, it is impossible to solve the Navier–Stokes and continuity equations analytically. Reynolds stress originating from the time averaging process was a problem that required a time-averaged Navier–Stokes equation (Reynolds averaged Navier–Stokes equations, RANS), along with turbulent models, to resolve. The fundamental mathematical equations that control computational fluid dynamics are the equations of continuity (conservation of mass), the equation of momentum (Navier–Stokes equation), and the equation of energy (conservation of energy). Only the continuity and momentum equations out of these governing equations are important for automotive flow problems involving external aerodynamic flow. Combining the transient term with the advection/convection term results in the following representation of the continuity equation:

$$\frac{\partial \rho_\infty}{\partial t} + \frac{\partial (\rho_\infty u_j)}{\partial x_j} = 0, \tag{6}$$

where ρ_∞ is the density of air, t is the time, x_j are the Cartesian coordinates and u_j are the components of air velocity in x_j-direction ($j = 1, 2, 3$).

The transient, advection/convection, diffusion, and source terms can be used to present the momentum equation as

$$\frac{\partial \rho_\infty u_i}{\partial t} + \frac{\partial (\rho_\infty u_j u_i)}{\partial x_j} = \frac{\partial}{\partial x_j} \left(\mu \frac{\partial u_i}{\partial x_j} \right) + S_i \,, \tag{7}$$

where μ is the viscosity and S_i is the user-defined source term.

The mean flow impact is more prominent in a real-world automobile flow problem. Therefore, a statistical method is employed for the vast majority of flow issues including turbulence by time averaging the momentum

and continuity equation to account for the mean velocity of the flow. The instantaneous flow velocity is split into mean velocity (U_i) and variable velocity (u_i') components using the time-averaging approach as

$$u_i = U_i + u_i' \,. \tag{8}$$

The Navier–Stokes equation is then created by converting the momentum equation to its simpler conserved version, which is

$$\frac{\partial u_i}{\partial t} + u_j \frac{\partial(\rho_\infty u_i)}{\partial x_j} = -\frac{1}{\rho_\infty}\frac{\partial p}{\partial x_i} + \frac{1}{\rho}\frac{\partial}{\partial x_j}\left(\mu \frac{\partial u_i}{\partial x_j}\right) + S_i \,, \tag{9}$$

where the diffusion term in its original form is written as

$$\frac{1}{\rho_\infty}\frac{\partial}{\partial x_j}\left(\mu \frac{\partial u_i}{\partial x_j}\right) = \frac{1}{\rho_\infty}\frac{\partial}{\partial x_j}\left(2\mu S_{ij} - \frac{2}{3}\mu \frac{\partial u_i}{\partial x_i}\delta_{ij}\right), \tag{10}$$

where S_{ij} denotes the strain tensor components and δ_{ij} is the stress sensor. The last term on the right side of the equation denotes the impact of volume dilation.

After averaging the mean and variable velocity components over time, the Reynolds averaging Navier–Stokes equation is produced and is represented as

$$\begin{aligned}\frac{\partial \overline{u}_i}{\partial t} + \overline{u_j \frac{-\partial\left(\rho_\infty \overline{u}_i\right)}{\partial x_j}} &= -\frac{1}{\rho_\infty}\frac{\partial \overline{p}}{\partial x_i} \\ &+ \frac{1}{\rho_\infty}\frac{\partial}{\partial x_j}\left(2\mu S_{ij} - \frac{2}{3}\mu \frac{\partial u_i}{\partial x_i}\delta_{ij}\right) + \frac{\partial}{\partial x_j}\left(-\rho_\infty \overline{u_i' u_j'}\right) + S_i \,,\end{aligned} \tag{11}$$

where $\overline{-u_i u_j}$ is the Reynolds stress term, here the over-bar denotes a time averaged quantity and prime denotes the deviation from the average.

The corresponding time-averaged continuity equation can then be written as

$$\frac{\partial u_j}{\partial x_j} = 0. \tag{12}$$

The system of equations for a three-dimensional flow consists of three RANS equations and a continuity equation, for a maximum of four equations. Four equations, however, require the system to be closed up for ten unknowns. One mean pressure, three mean velocities, and six Reynolds stresses make up this. As a result, more equations are required to finish the

system. By simulating the Reynolds stress factor in the RANS equation, the closure of the system can be achieved. This also goes by the name of 'turbulence modelling'. The turbulence model employed will have an impact on how realistically the RANS equations represent the flow [15]. The governing equations for kinetic energy and dissipation in the RNG k-ε model are as follows:

Equation of turbulent kinetic energy

$$\frac{1}{\sqrt{g}}\frac{\partial}{\partial t}\left(\rho_\infty x\sqrt{g}\right)+\frac{\partial}{\partial u_j}\left(\rho_\infty \overline{u}_j x-\frac{u_{\text{eff}}}{\sigma_k}\frac{\partial x}{\partial x_j}\right) = \mu_t\left(P+P_B\right)-\rho_\infty\varepsilon-\frac{3}{2}\left(\mu_t\frac{\partial u_i}{\partial x_i}+\rho_{\infty_x}\right)\frac{\partial u_i}{\partial x_i}, \tag{13}$$

where

$$\mu_{\text{eff}}=\mu+\mu_t\,,$$
$$P=2S_{ij}\frac{\partial u_i}{\partial x_j}\,,$$
$$P_B=-\frac{g_i}{\sigma_{h,t}}\frac{1}{\rho_\infty}\frac{\partial \rho_\infty}{\partial x_i}$$

and $\sqrt{g}$ is the determinant of the metric tensor, g_i is the component of the gravitational vector in the ith direction, x is the coordinate along X-axis, μ_{eff} is the effective viscosity, and μ_t is the turbulent viscosity, σ_k is the turbulent Prandtl numbers for k, $\sigma_{h,t}$ is the k-ε turbulence model coefficient, ε is the rate of dissipation, and ρ_∞ is the density of air:

$$\begin{aligned}\frac{1}{\sqrt{g}}\frac{\partial}{\partial t}\left(\sqrt{g}\rho_\infty\varepsilon\right)+\frac{\partial}{\partial u_j}\left(\rho_\infty\overline{u}_j\varepsilon-\frac{u_{\text{eff}}}{\sigma_\varepsilon}\frac{\partial\varepsilon}{\partial x_j}\right) &= C_{\varepsilon l}\frac{\varepsilon}{x}\left\{\mu_t\left(P+C_{\varepsilon 3}P_B\right)\right\}-C_{\varepsilon 4}\rho_\infty\varepsilon\frac{\partial u_i}{\partial x_i}\\ &-\frac{2}{3}C_{\varepsilon 1}\frac{\varepsilon}{x}\left(\mu_t\frac{\partial u_i}{\partial x_i}+\rho_\infty x\right)\frac{\partial u_i}{\partial x_i}\\ &-C_{\varepsilon 2}\frac{\varepsilon^2}{x}-\frac{C_\mu\eta^3\left(1-\frac{\eta}{\eta_0}\right)}{1+\beta\eta^3}\frac{\rho_\infty\varepsilon^2}{x}\,,\end{aligned} \tag{14}$$

where $\eta=S\dfrac{x}{\varepsilon}$, $S=\left(2S_{ij}S_{ij}\right)^{1/2}$, S is the magnitude of the rate of strain, σ_ε is the turbulent Prandtl number for ε, $C_{\varepsilon l}$, $C_{\varepsilon 1}$, $C_{\varepsilon 2}$, $C_{\varepsilon 3}$, and $C_{\varepsilon 4}$ are constants, η_0 is the creeping viscosity, β is the coefficient of thermal expansion. The RNG theory gives values of the constants [16].

Ansys software was used for the numerical analysis [20]. In order to create a three dimensional CAD model Solidworks software was used [21]. Complete surface and wireframe data were produced. The Initial Graphics Exchange Standard (IGES) format was then used to translate this data [21]. The vehicle used in the CFD simulations is depicted in detail in Fig. 8.

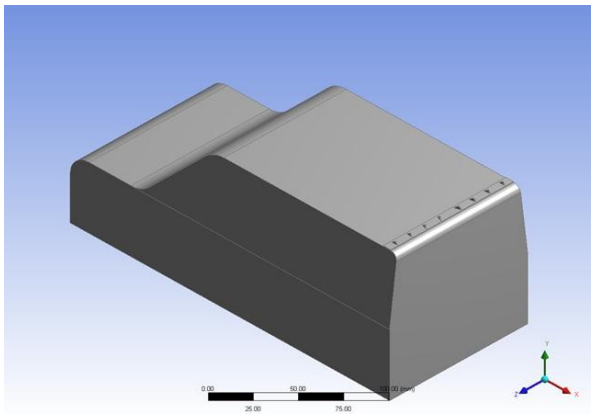

Figure 8: CAD model of the vehicle.

The CAD model of the car was improved using Ansys geometry modeller because the model had an excessive number of intersecting surfaces and free edges. The computational space has the following measurements: 1.5 times the height above the ground, 3 times the breadth sideways, 5 times the body length downstream, and 3 times the length upstream. A suitable number of grid points were assigned to each subblock of the computational domain after it had been partitioned into many logical blocks. The domain was split in half using a symmetry plane to reduce calculation time, and the resulting meshes had 1.1 million fluid cells. For each of the many wind tunnel domains, a different meshing characteristic was used.

Despite the varied approaches, both domains utilised the same arrangement of hexahedral core cells. These components are easily adaptable to the intricate bodies used in aerospace and automotive bodies. The utility vehicle utilised in the experiment's original 1/15th scale model was utilised. The ICEM Meshing tool from Ansys was used to complete the meshing. The vehicle's meshed geometry is depicted in Fig. 9.

Before starting the simulations, the solver setup must be finished for the numerical analysis issue. The viscosity model, boundary condition, solution controls, and solver type (3D or 2D) are all included in the solver settings.

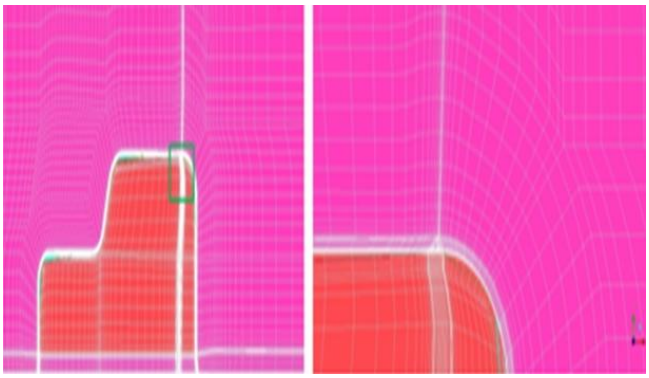

Figure 9: Meshed geometry of the vehicle.

The terms 'velocity inlet' and 'pressure outlet' are used to describe the inlet and outlet of a wind tunnel, respectively. The temperature and density of the typical ambient environment were taken into consideration when calculating the fluid characteristics. In the near-wall region, a typical wall function was used. At the input of the flow domain, the mass flow rate and static pressure were imposed. When the total momentum residuals had decreased by at least three orders of magnitude and the monitored flow velocities and flow characteristics had not significantly changed after additional iterations, the calculations were stopped. On a machine with 32 GB of RAM and 16 parallel processors, the typical solution time for a mesh with 1.1 million cells was roughly 36 hours.

3 Results and discussions

3.1 Experimental results

Variations of pressure coefficient, dynamic pressure, coefficient of drag and coefficient of lift for different arrangements of VG's with different I/H ratios at different free stream velocities are presented in this section.

3.1.1 Pressure coefficient

Figure 10 depicts the pressure coefficient change along the scale model's x coordinates at a free stream velocity of 2.42 m/s. From the figure, it can be seen that the pressure coefficient value without VG is lowest at the x coordinate of around 240 mm, while it is at its highest when VG has an

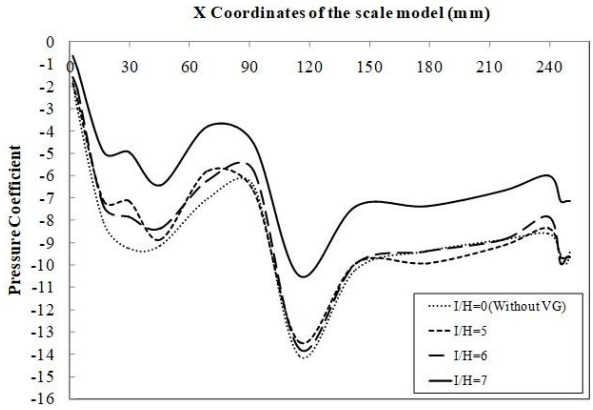

Figure 10: Variation of C_p at $U_\infty = 2.42$ m/s for different values of I/H ratio.

I/H ratio of 6. This is because the boundary layer's thickness is almost identical to the I/H ratio of 6. Figures 11, 12, and 13 depict the pressure coefficient change along the scale model's x coordinates at corresponding free stream velocities of 3.7, 5.42, and 7.14 m/s. It is clear that for different values of the I/H ratio, the values of the pressure coefficient do not change appreciably as the velocity increases. This is due to the inverse relationship between the boundary layer thickness and Reynolds number, which means that at higher velocities, or higher Reynolds number, the boundary layer thickness becomes too tiny and prevents the effect of the I/H ratio of VG from being realised.

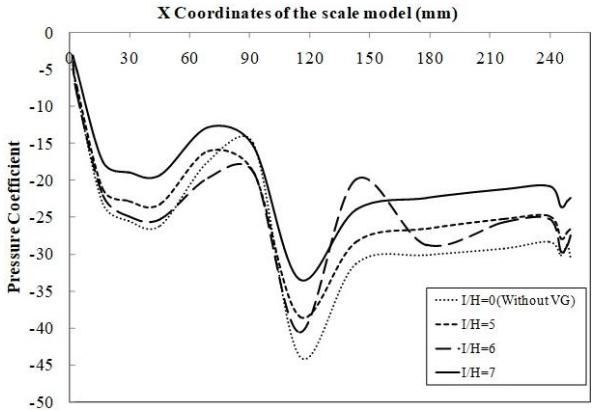

Figure 11: Variation of C_p at $U_\infty = 3.7$ m/s for different values of I/H ratio.

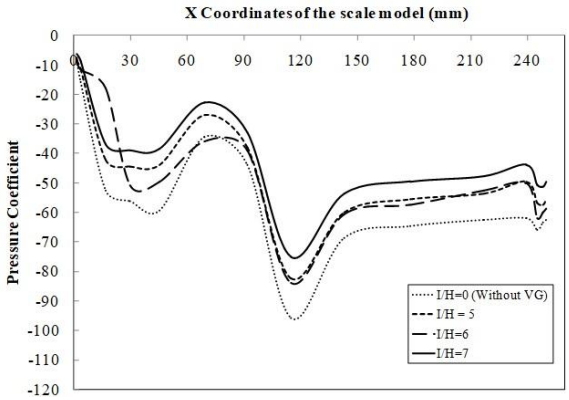

Figure 12: Variation of C_p at $U_\infty = 5.42$ m/s for different values of I/H ratio.

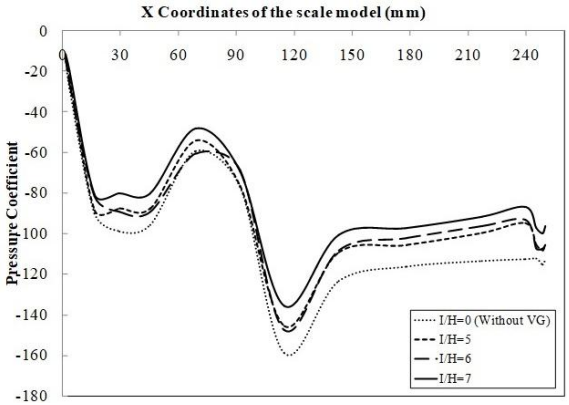

Figure 13: Variation of C_p at $U_\infty = 7.14$ m/s for different values of I/H ratio.

It is intriguing to note that the presence of VG can raise the pressure coefficient by about 18% at a speed of 7.14 m/s. Similarly, with an I/H ratio of 6, adding VG can raise the pressure coefficient to a maximum of approximately 26% and 20% at velocities of 5.42 and 3.7 m/s, respectively.

3.1.2 Dynamic pressure

Figure 14 depicts the dynamic pressure variation along the scale model's x coordinates at a free stream velocity of 2.42 m/s. From the figure, it can be seen that dynamic pressure without VG is largest at the x coordinate of around 240 mm, whereas dynamic pressure with VG having an I/H ratio

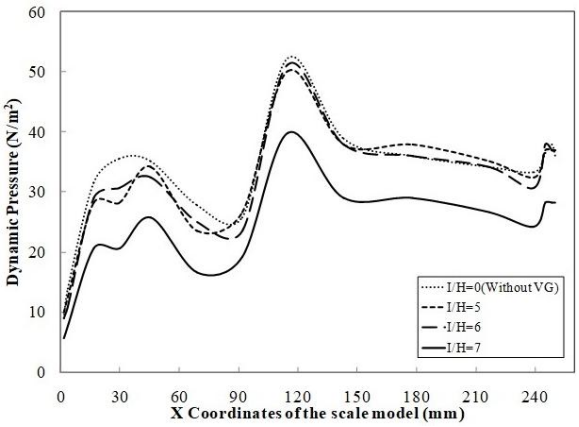

Figure 14: Variation of P_d at $U_\infty = 2.42$ m/s for different values of I/H ratio.

of 6 is smallest. The findings demonstrate that adding VG enhances the dynamic pressure over the surface of the car roof, which is advantageous for preventing flow separation and the ensuing losses. Figures 15, 16, and 17 illustrate the dynamic pressure change along the scale model's x coordinates at different free stream velocities of 3.7, 5.42, and 7.14 m/s. It is clear that for different values of the I/H ratio, the dynamic pressure values do not change considerably as the velocity increases. It is intriguing to note that the incorporation of VG can raise the dynamic pressure by about 21% at a speed of 7.14 m/s. Similar to this, the presence of VG can raise

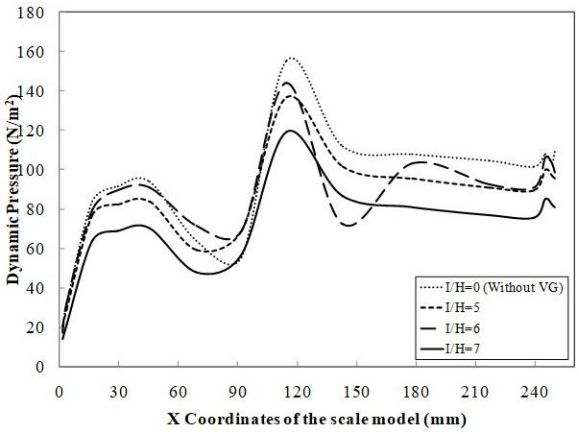

Figure 15: Variation of P_d at $U_\infty = 3.7$ m/s for different values of I/H ratio.

the dynamic pressure to a maximum of approximately 24% and 18% at velocities of 5.42 and 3.7 m/s, respectively, for an I/H ratio of 6.

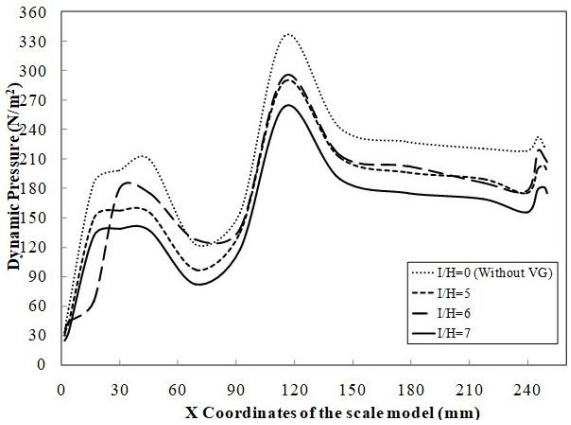

Figure 16: Variation of P_d at $U_\infty = 5.42$ m/s for different values of I/H ratio.

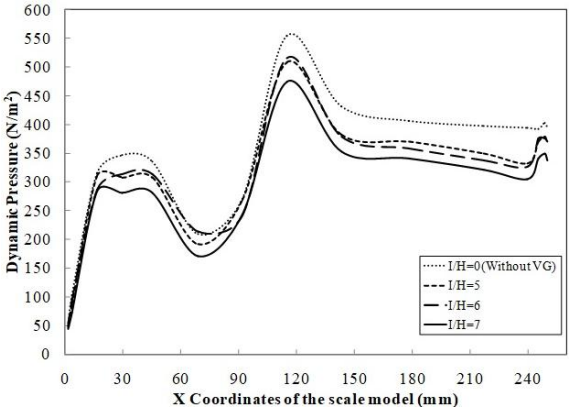

Figure 17: Variation of P_d at $U_\infty = 7.14$ m/s for different values of I/H ratio.

3.1.3 Coefficient of drag

Figure 18 depicts the variance in C_D values for various I/H ratio values at various free stream velocities along the scale model's longitudinal centre line. The graphic makes it very clear that the addition of VG lowers the value of C_D. This can be attributable to the use of VG to prevent flow separation. For instance, using VG with an I/H ratio of 6 reduces the

coefficient of drag at a velocity of 2.42 m/s by up to 90% compared to the results obtained without VG. For VG with an I/H ratio of 5, a minimum 20% reduction in drag is obtained at the same velocity. The C_D stays constant as velocity increases for changing I/H ratio values. However, when the I/H ratio is raised, the C_D values change as the velocity rises. We conclude that VG with an I/H ratio of 6 will be effective at lower speeds.

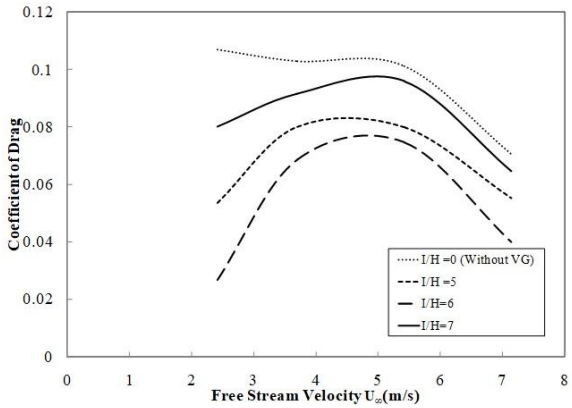

Figure 18: Variation of C_D for different values of I/H ratio along the centre plane.

3.1.4 Coefficient of lift

Figure 19 depicts the change in C_L values along the scale model's longitudinal centre line for various I/H ratio values and free stream velocities.

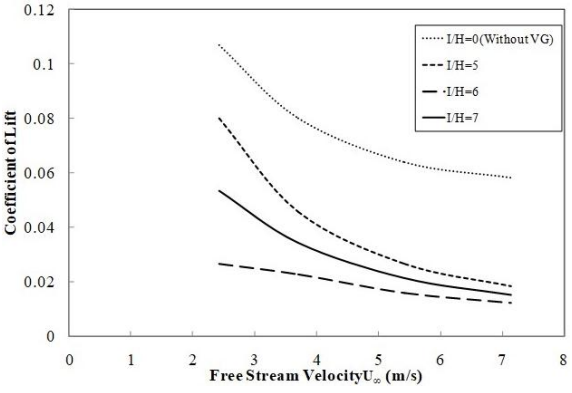

Figure 19: Variation of C_L for different values of I/H ratio along the centre plane.

The graphic makes it very clear that the inclusion of VG lowers the value of C_L. This can be attributable to the use of VG to prevent flow separation. For instance, when VG with an I/H ratio of 6 is utilised, the coefficient of lift is lowered by up to 87% at a velocity of 2.42 m/s compared to the results obtained without VG. For VG with an I/H ratio of 5, a minimum loss in the lift of 50% is attained at the same velocity. However, as velocity increases both with and without VG, C_L's value declines. The findings showed that for all VGs of I/H ratios at greater velocities, C_L remained constant.

3.2 CFD simulations

The variation of pressure contour and velocity contour along the x/L ratio at different free stream velocities for different arrangements of VG's with different I/H ratios are presented.

3.2.1 Validation of CFD results

Experimental absolute pressure measurement from baseline testing (experiments without VG) at 7.14 m/s was compared with the simulated results for validation purposes. The front body absolute pressure shows a minor variance, but the pattern of the plot is comparable, even though the findings of the absolute pressure on the roof surface closely match the experimental data as in Fig. 20. The front windshield of the car model has the highest

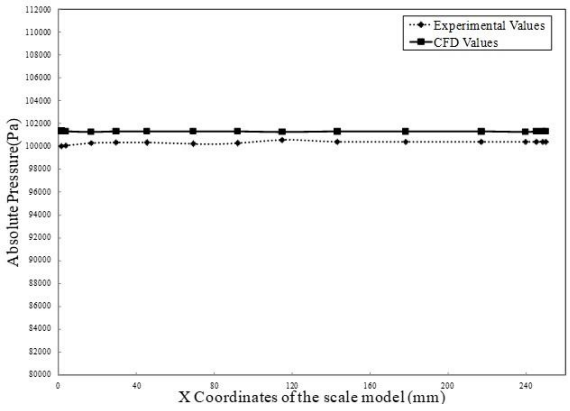

Figure 20: Comparison of experimental and CFD values of absolute pressure along the centre line of vehicle surface at a velocity of 7.14 m/s.

absolute pressure value. The simulation's calculation of the maximum absolute pressure on the front windshield came out at 101.676 kPa, which is fairly close to the experimental measurement of 100.586 kPa.

3.2.2 Pressure contour

The results of the CFD simulation of the variation in absolute pressure at the utility vehicle's rear top surface with and without VG are shown in Fig. 21a and 21b, respectively. It may be concluded that there is little difference between the two scenarios in the absolute pressure value at the utility vehicle's rear top surface. According to the analysis, the vortex generator energises the flow and causes it to separate at a distance that is comparatively greater than that of the vehicle model without a vortex generator, which lowers the drag of the vehicle.

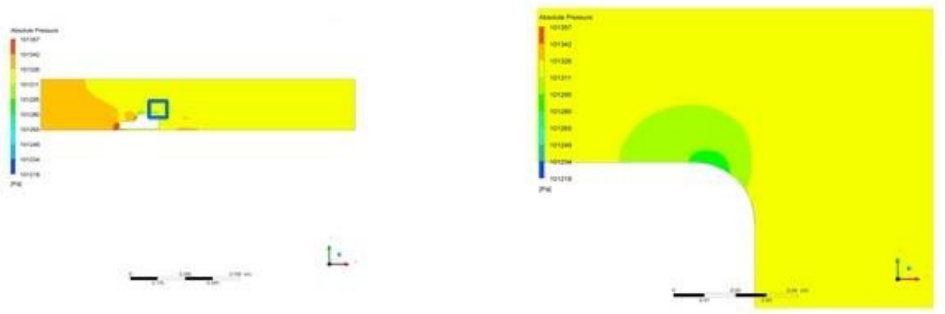

(a)

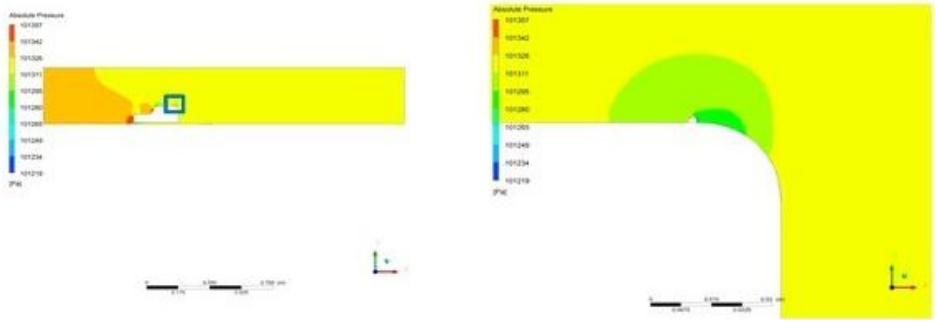

(b)

Figure 21: Pressure contour on the vehicle without (a) and with (b) vortex generators at a velocity of 7.14 m/s.

3.2.3 Velocity contour

The results of the CFD simulation (using Ansys Tool Package 2020) of the fluctuation in velocity at the utility vehicle's rear top surface with and without VG are shown in Fig. 22a and 22b, respectively. The velocity at the front end of the car is assumed to be relatively low, however, it is discovered that the velocity at the rear end of the car is higher than that at the front end. This demonstrates how low the pressure is at the vehicle's back. It has been accomplished with the help of the incorporation of vortex generators, and the drag has also been decreased. The velocity at the rear of the car will be minimized if the pressure drop is lowered. When compared to the vehicle model without vortex generators, the graphic depicts the velocity at the rear end that has less wake. This always results in the vehicle's drag being reduced. This backs up the experimental results covered in Section 3.1.2 that the addition of VG is beneficial for preventing flow separation and the ensuing losses.

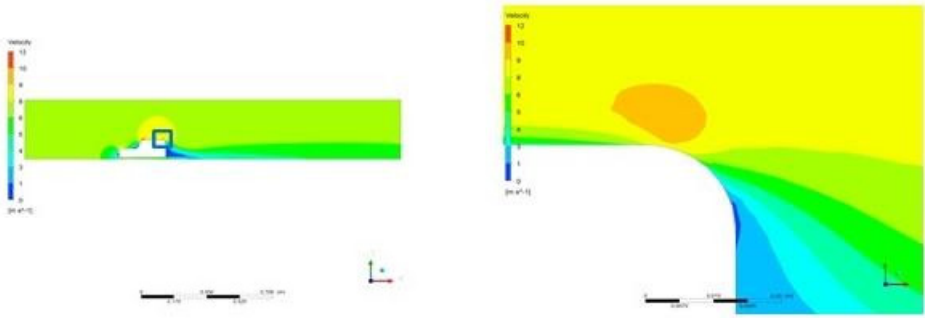

(a)

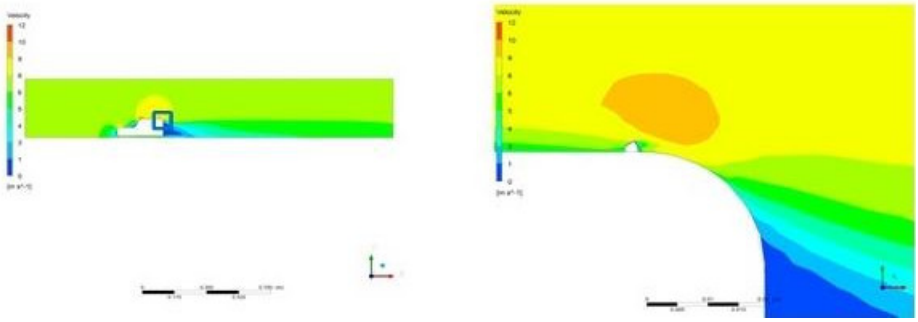

(b)

Figure 22: Velocity contour on vehicle without (a) and with (b) vortex generators at a velocity of 7.14 m/s.

4 Conclusion

The following conclusions were drawn from an experimental study on the measurement of the variation of dynamic pressure and pressure coefficient on the roof of a utility vehicle with and without vortex generators (VG).

The value of the pressure coefficient without vortex generators VG is minimum, whereas its value was observed to be maximum with VG having an I/H ratio of 6. The addition of VG can raise the pressure coefficient by roughly 17% at a speed of 2.42 m/s. For different values of the I/H ratio, the values of the pressure coefficient do not change all that much as the velocity increases.

The addition of VG raises the dynamic pressure over the surface of the vehicle roof, which is advantageous for preventing flow separation and the ensuing losses. At a velocity of 2.42 m/s, the inclusion of VG reduces the value of C_D by 90%, and VG achieves a minimum drag reduction of 20% with an I/H ratio of 5. It is noted that VG with a 6 I/H ratio will be helpful at lower velocities. The results showed that at a higher velocity, the value of C_L remains constant for VG with varied values of the I/H ratio. The value of C_L declines with the rise in velocity both with and without VG.

The pressure contour of the CFD analysis demonstrates that the vortex generator energises the flow and causes the flow to separate at a distance that is significantly greater than that of the vehicle model without the vortex generator, which lowers the drag of the vehicle. When compared to the vehicle model without vortex generators, the velocity contour of the CFD study demonstrates that the velocity at the rear end has reduced wake.

Received 17 April 2023

References

[1] Lishu H., Bao H., Yongwei G., Binbin W.: *Effect of vortex generator spanwise height distribution pattern on aerodynamic characteristics of a straight wing.* Adv. Aerodyn. **5**(2023), 1, 1–15. doi: 10.1186/s42774-023-00137-1

[2] Nilavarasan T, Joshi G.N., Misra A., Manisankar C., Verma S.B.: *Spatial and temporal alterations due to vortex generators in a flare induced shock–boundary layer interaction.* Eur. J. Mech. B-Fluid. **99**(2023), 3, 98–115. doi: 10.1016/j.euromechflu.2023.01.007

[3] Jana T., Kaushik M.: *Survey of control techniques to alleviate repercussions of shock-wave and boundary-layer interactions*. Adv. Aerodyn. **27**(2022), 4, 1–30. doi: 10.1186/s42774-022-00119-9

[4] Kung M.C., Kao C.S., Keh C.C.: *The effect of vortex generators on shock-induced boundary layer separation in a transonic convex-corner flow*. Aerospace **157**(2021), 8, 1–11. doi: 10.3390/aerospace8060157

[5] Hadi B., Seyed Ali A.M., Seyed Amir A.O., Mohammad R.S.: *Effects of micro-vortex generators on shock wave structure in a low aspect ratio duct, numerical investigation*. Acta Astronaut. **178**(2021), 1, 616–624. doi: 10.1016/j.actaastro.2020.08.012

[6] Neeraj K.G., Nirmal K.S.: *Control of shock-induced separation inside air intake by vortex generators*. Heat Transfer **51**(2022), 1, 766–788. doi: 10.1002/htj.22329

[7] Azam C.I., Mohd R.S., Konstantinos K.: *Potential of micro-vortex generators in enhancing the quality of flow in a hypersonic inlet-isolator*. J. Adv. Res. Fluid Mech. Therm. Sci. **77**(2021), 1, 1–10. doi: 10.37934/arfmts.77.1.110

[8] Tian L., Hao L., Jie Z., Jiye Z.: *Numerical study on aerodynamic resistance reduction of high-speed train usingvortex generator*. Eng. Appl. Comput. Fluid Mech. **17**(2023), 1, 1–17. doi: 10.1080/19942060.2022.2153925

[9] Arunvinthan S., Raatan V.S., Nadaraja Pillai S., Amjad A.P., Rahman M.M, Khalid A.J.: *Aerodynamic characteristics of shark scale-based vortex generators upon symmetrical airfoil*. Energies **14**(2021), 1808, 1–22. doi: 10.3390/en14071808

[10] Gnatowska R., Gajewska K., Kańtoch R.: *Numerical calculations of VGs influence on aerodynamic characteristics of airfoil*. Acta Phys. Pol. A **139**(2021), 5, 1, 586–589. doi: 10.12693/APhysPolA.139.586

[11] Tavernier D., Ferreira C., Viré A., LeBlanc B., Bernardy S.: *Controlling dynamic stall using vortex generators on a wind turbine airfoil*. Renew. Energ. **172**(2021), 7, 1194–1211. doi: 10.1016/j.renene.2021.03.019

[12] Wu Z., Chen T., Wang H., Shi H.: *Investigate aerodynamic performance of wind turbine blades with vortex generators at transition area*. Wind Eng. 4**6**(2022), 615–629. doi: 10.1177/0309524X211038542

[13] Reza B., Milad R., Mohammad R.S.: *Numerical simulations of spoiler's effect on a hatchback and a sedan car exposed to crosswind effect*. J. Appl. Comput. Mech. **9**(2023), 2, 346–356. doi: 10.22055/JACM.2021.36955.2937

[14] Viswanathan H.: *Aerodynamic performance of several passive vortex generator configurations on an Ahmed body subjected to yaw angles*. J. Braz. Soc. Mech. Sci. Eng. **43**(2021), 2, 1–23. doi: 10.1007/s40430-021-02850-8

[15] Popp M., White C.F., Bernal D., Wainwright D.K., Lauder G.V.: *The denticle surface of thresher shark tails: Three-dimensional structure and comparison to other pelagic species*. J. Morphol. **281**(2020), 6, 938–955. doi: 10.1002/jmor.21222

[16] SAE: *Wind tunnel test procedure for trucks and buses, Recommended practice*. SAE J. **1252_201**207(2012).

[17] Li X., Yang K.,.Wang X.: *Experimental and numerical analysis of the effect of vortex generator height on vortex characteristics and airfoil aerodynamic performance*. Energies **12**(2019), 5, 1–19. doi: 10.3390/en12050959

[18] Szwaba R., Hinc K., Ochrymiuk T., Krzemianowski Z., Doerffer P., Kurowski M.: *Open low speed wind tunnel – design and testing*. Arch. Thermodyn. **42**(2021), 1, 57–70. doi: 10.24425/ather.2021.136947

[19] Barlow J.B., Rae Jr. W.H., Pope A.: *Low-Speed Wind Tunnel Testing* (3rd Edn.). Wiley, 2010.

[20] Koprowski A., Rzadkowski R.: *Computational fluid dynamics analysis of 1 MW steam turbine inlet geometries*. Arch. Thermodyn. **42**(2021), 1, 35–55. doi: 10.24425/ather.2021.136946

[21] Pazouki A., Radu S., Dan N.: *A high performance computing approach to the simulation of fluid-solid interaction problems with rigid and flexible component*. Arch. Mech. Eng. **61**(2014), 2, 227–251. doi: 10.2478/meceng-2014-0014